Journal of Electronic Materials, Vol. 10, No. 6, 1981

THE PSEUDOBINARY HgTe-CdTe PHASE DIAGRAM*

F. R. Szofran and S. L. Lehoczky

McDonnell Douglas Research Laboratories

St. Louis, MO 63166

(Received May 11, 1981)

The complete pseudobinary HgTe-CdTe constitutional phase diagram was determined by precision differential-thermal-analysis measurements and used to calculate the segregation coefficient of Cd as a function of Cd concentration and interface temperature. A thorough error analysis was made, and the results are compared with published data. Empirical, analytical-expressions were developed for the liquidus and solidus compositions as functions of temperature to facilitate calculations of phase equilibrium parameters.

Key words: mercury cadmium telluride, phase diagram, compound semiconductor, differential thermal analysis, segregation or distribution coefficient

Introduction

In order to grow high-quality $Hg_{1-x}Cd_xTe$ crystals by unidirectional solidification techniques, the pseudobinary HgTe-CdTe constitutional phase diagram must be accurately known. Previously published results[1-5] either do not cover the entire composition range or are not accurate enough for modeling the growth process. In this study the complete pseudobinary phase diagram was accurately determined by making differential thermal analysis (DTA) measurements. The Cd segregation coefficient calculated from this phase diagram

* *Work supported in part by NASA contract NAS8-33107 and in part by the McDonnell Douglas Corporation Independent Research and Development program.*

0361-5235/81/1100-1131$03.00/1

was then used successfully to model[6] the axial compositional variations in alloys grown by the Bridgman-Stockbarger method.[7]

Alloy Preparation

For the phase diagram measurements, the HgTe-CdTe alloys were prepared by reacting the constituent elements in sealed, fused-silica, 5-mm i.d. x 10-mm o.d. ampules. The ampules were cleaned and etched in aqueous HF and annealed at 1150°C in vacuum to remove residual contaminants. Square cross-section bars of 99.9999% pure Cd and Te were cut from large ingots. The Cd bars were etched in concentrated HNO_3 and repeatedly rinsed in methanol. Similarly, the Te bars were etched in Br_2 and also rinsed repeatedly in methanol.

The ampules were then loaded in a vertical position with 99.99999% pure Hg first, then Te, and finally Cd. This procedure prevented contact between Hg and Cd in the presence of air. The ampules were evacuated and backfilled with He several times before final evacuation and sealing.

Using the above procedure, little or no wetting occurred between the ampule and the alloy during reaction of the elements. In many cases, the reacted alloy would slide inside the ampule. The alloy constituents are listed in Table I for the samples for which data are reported.

Experimental Method for Differential Thermal Analyses

DTA measurements were used for determining the phase equilibrium temperatures. The experimental arrangement of the ampules in the DTA furnace is shown in Fig. 1.

An ampule containing the alloy sample was mounted coaxially with a second ampule inside the 460-mm long isothermal furnace liner (Na heat-pipe)

Table I. Elemental constituents of alloys used for the phase diagram determination. Mass measurement accuracy is ± 0.6 mg.

Composition (x)	Hg (g)	Cd (g)	Te (g)	Stoichiometric Hg (g)	Excess Hg (mg)
0.1	10.8349	0.6732	7.6555	10.8345	0.4
0.2	9.6299	1.3501	7.6570	9.6289	1.0
0.3	9.5487	2.2950	8.6748	9.5428	5.9
0.4	7.2201	2.6992	7.6555	7.2190	1.1
0.6	4.5719	3.8343	7.2582	4.5687	3.2
0.7	3.6452	4.7582	7.7183	3.6433	1.9
0.8	4.7977	10.7427	15.2430	4.7939	3.8
0.9	2.4093	12.1474	15.3200	2.4083	1.0

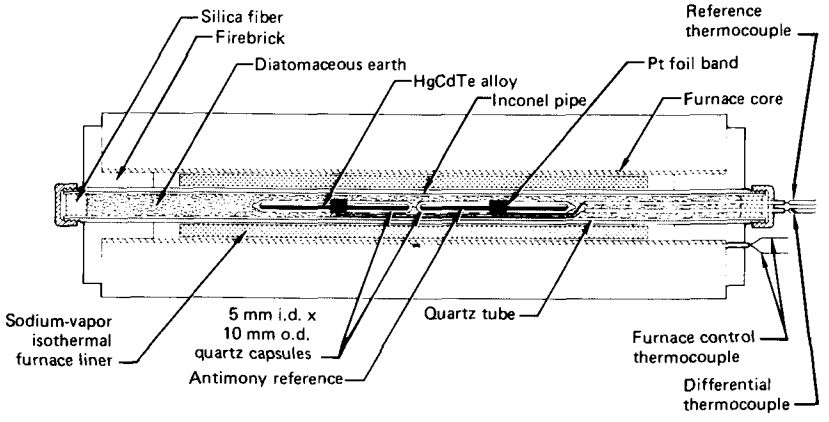

Fig. 1 Experimental arrangement for differential-thermal-analysis measurements.

and the 610-mm long tube furnace. The second ampule contained antimony, which served as the reference heat capacity and provided a thermocouple calibration point for each experimental run. The ampules were held on axis by a quartz centering fixture (not shown in the figure). The annular volume between the ampules and a 25-mm o.d. quartz tube was filled with powdered diatomaceous earth. The 25-mm tube was inside an Inconel tube to prevent damage to the heat pipe and furnace in case of ampule failure.

Both the alloy and Sb-reference ampules were fitted with a 5-mm wide Pt-foil band positioned axially near the middle of the ampule. The two junctions of a type-K differential thermocouple were affixed to the bands. A separate type-K thermocouple was fastened to the Pt band on the Sb-reference ampule. Each thermocouple lead extended to a copper junction maintained in a triple-point-of-water cell.

A block diagram of the furnace control and data acquisition instrumentation is shown in Fig. 2. Using an x-y recorder, the temperature of the Sb-reference sample was monitored on the x-axis, and the differential thermocouple output was measured on the y-axis.

For data recording, all graph paper was calibrated by drawing vertical lines at 1-mV intervals using a potentiometer (Leeds and Northrop model 8691). This potentiometer was periodically checked against another potentiometer (Leeds and Northrop K-4) and verified to be accurate within $\pm$ 20 μV. The output of a type-K thermocouple is approximately 40 μV/°C.

A temperature programmer was used to change the furnace temperature at a uniform rate and turn the x-y recorder servo and pen-lift on and off. The furnace protection circuit, a meter relay that drives a power relay, provided an additional margin of safety against excessive furnace temperatures.

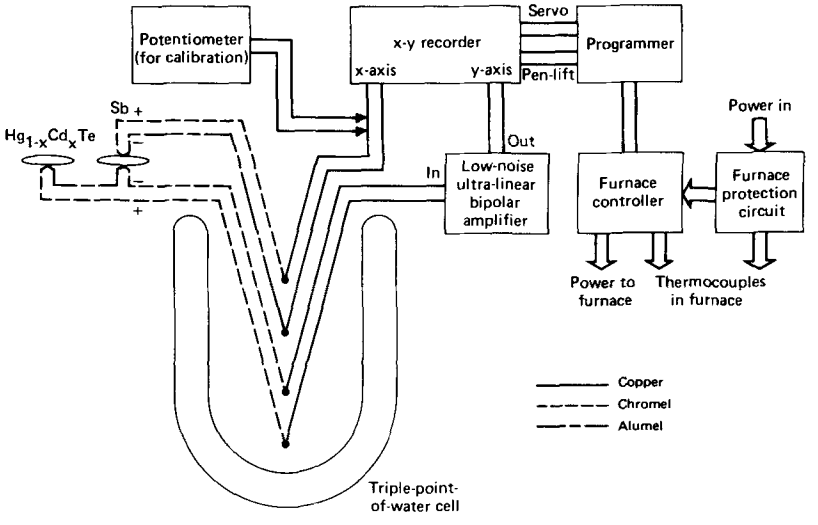

Fig. 2 Electronic instrumentation for differential thermal analysis.

A thermocouple calibration facility was constructed similar to that described in Ref. 8 and used graphite crucibles and NBS reference materials.[8] The melting-temperature reference materials were Zn, Al, and Cu. The melting temperature of the Sb-reference sample served as an internal calibration temperature, and the Sb melting point was checked at least once before each run.

Differential-Thermal-Analysis Results

For DTA measurements, higher rates of heating or cooling yield a larger signal and thus a better signal-to-noise ratio. Measurements made at excessive heating or cooling rates, however, may not reflect true equilibrium values. To ensure that the heating and cooling rate used in this study was within the allowable range, test runs were made with a HgTe calibration sample at a series of heating rates (0.5, 1, 2, 3, 4, and 5°C/min). The DTA curves for HgTe are shown in Fig. 3. The melting temperatures are within ± 1.7°C of 669.5°C for all heating rates, and there is no evidence for systematic variation of the onset of thermal-arrest with heating rate. Because the maximum cooling rate of the furnace below 670°C was about 3°C/min, all alloy heating and cooling curves were recorded at a rate of 2°C/min to enhance the differential thermocouple outputs while allowing identical heating and cooling rates for all specimens. In Fig. 3, the seeming inconsistency among the cooling curves and in the 3°C/min heating curve is attributed to the horizontal attitude of the furnace during the HgTe measurements. The total mass of HgTe within the Pt-foil bands could change during the hot part of each cycle due to bubble motion. This phenomenon would affect only the magnitude of the signal and was eliminated subsequently by slightly tilting the furnace.

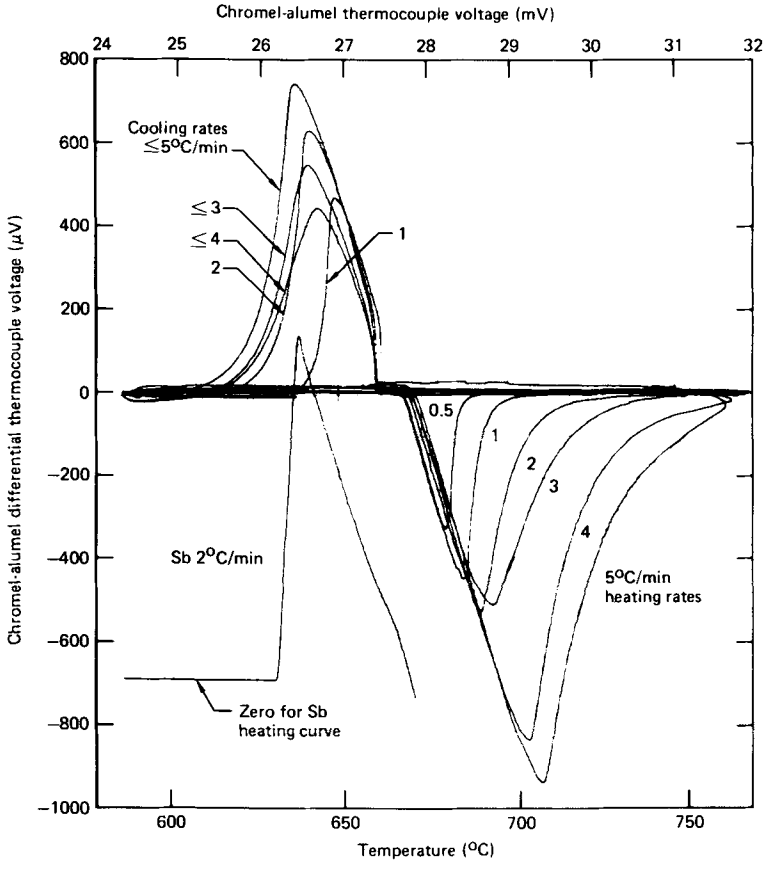

Fig. 3 Rate dependence of thermal arrest for HgTe.

Inhomogeneties in the alloys can introduce significant uncertainties into the phase equilibrium temperatures deduced from DTA. For this reason, the samples were always quenched following casting and cooled uniformly after each DTA run to reduce the possibility of preferential alloy segregation along the ampule axis. To eliminate radial alloy inhomogeneities, the samples were annealed at temperatures, T_A, just below their solidus values. To ascertain the minimum annealing times required, samples with mole fraction x = 0.1, 0.2, 0.8, and 0.9 were annealed for successively longer annealing times from 1 to 60 h, and a DTA run was made following each anneal. An increase in the annealing time from 1 to 15 h always resulted in a significant sharpening of the DTA curves in the vicinity of the apparent solidus temperatures, which indicates that the annealing effected alloy homogenization. In agreement with previous results,[9] the changes caused by increasing the annealing time beyond

30 h were usually negligible. These effects are shown for samples with x = 0.1 and 0.2 in Figs. 4 and 5, where T_A and T_L correspond to the annealing and liquidus temperatures. The symbols 1, 2, 3, and 4 designate the DTA curves that were obtained following annealing times of 1, 15, 30, and 60 h, respectively.

DTA curves are shown in Fig. 6 for $Hg_{1-x}Cd_xTe$ samples annealed ≥ 60 h with x = 0.1, 0.2, 0.3, 0.4, 0.6, 0.7, 0.8, and 0.9, and the collection of melting curves is shown in Fig. 7. The horizontal axis shows the measured temperature of the Sb-reference ampule, T, and the vertical axis gives differential temperatures, S, for the alloy ampule measured with respect to T.

Considering radiation heat transfer only, the heat balance equation at the outer wall of the sample ampule is

$$\epsilon_F T_F^4 - \epsilon_p T_1^4 = \frac{r_s}{r_q}(\epsilon_p T_1^4 - \epsilon_s T_s^4), \tag{1}$$

where T_F, T_1, and T_s are the furnace, sample thermocouple, and sample temperatures; ϵ_F, ϵ_s, and ϵ_p are the furnace, sample, and fused-silica emissivities;

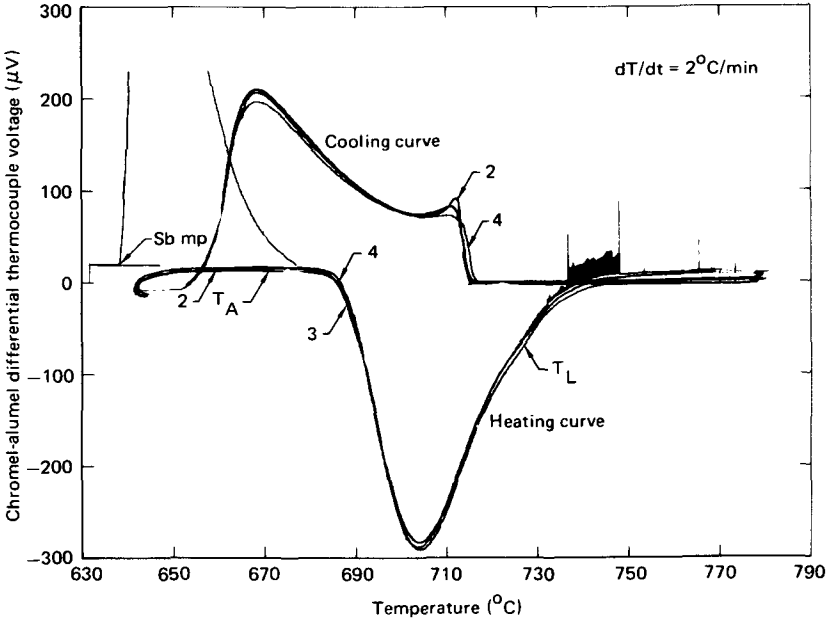

Fig. 4 Differential-thermal-analysis data for $Hg_{0.9}Cd_{0.1}Te$. Curves 2, 3, and 4 correspond to annealing times of 15, 30, and 60 h, respectively.

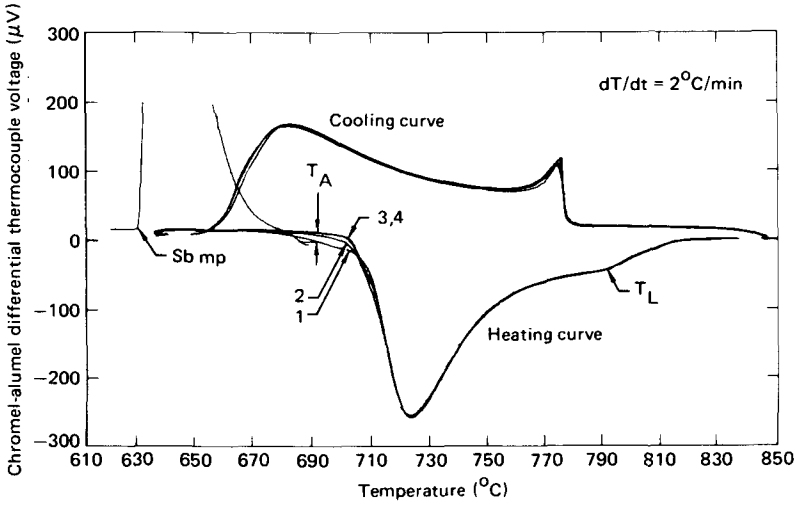

Fig. 5 Differential-thermal-analysis data for $Hg_{0.8}Cd_{0.2}Te$. Curves 1, 2, 3, and 4 correspond to annealing times of 1, 15, 30, and 60 h, respectively.

and r_s and r_q are the inner and outer radii of the ampules. The differential thermocouple signal is given by $S = T_1 - T$.

For steady-state conditions where the furnace temperature increases at a constant rate, $T = T_F + P'$, where P' is a constant. Using the approximations

$$T_1^4 = (T + S)^4 \approx T^4 + 4ST^3 \tag{2}$$

and

$$T_F^4 = (T + P')^4 \approx T^4 + 4P'T^3, \tag{3}$$

Eq. (1) yields

$$T_s^4 \approx T^4\left[\left(1 + \frac{r_q}{r_s}\right)\frac{\epsilon_p}{\epsilon_s} - \frac{r_q}{r_s}\frac{\epsilon_F}{\epsilon_s}\right] + 4ST^3\left(1 + \frac{r_q}{r_s}\right)\frac{\epsilon_p}{\epsilon_s} - 4P'T^3\frac{r_q}{r_s}\frac{\epsilon_F}{\epsilon_s}. \tag{4}$$

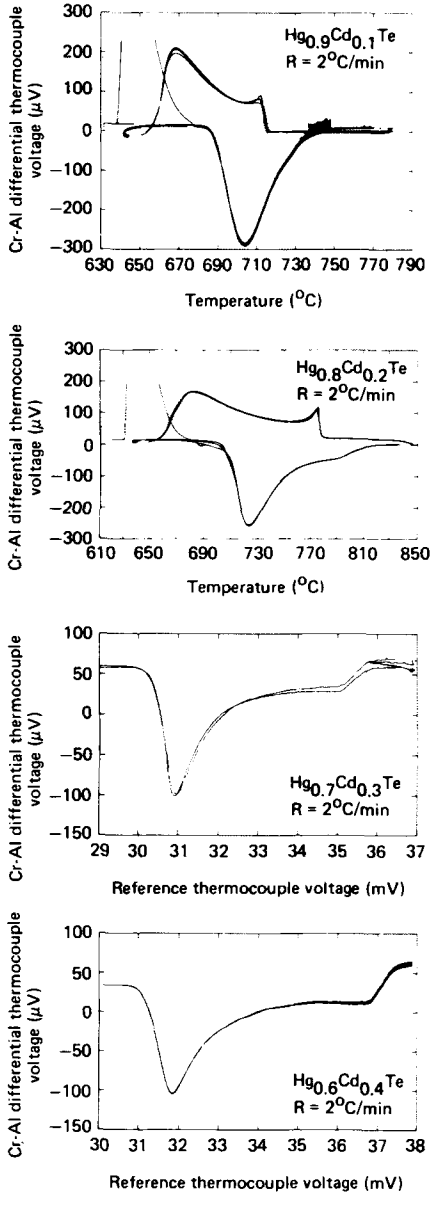

Fig. 6 **DTA data for x = 0.1, 0.2, 0.3, 0.4, 0.6, 0.7, 0.8 and 0.9 Hg_{1-x} Cd_dTe alloys. R is the heating and cooling rate.**

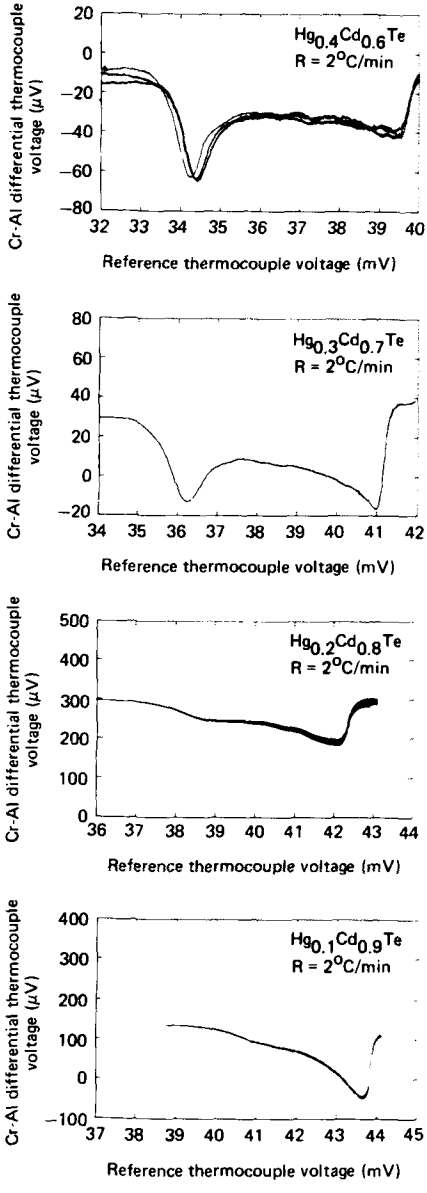

Fig. 6 (Continued)

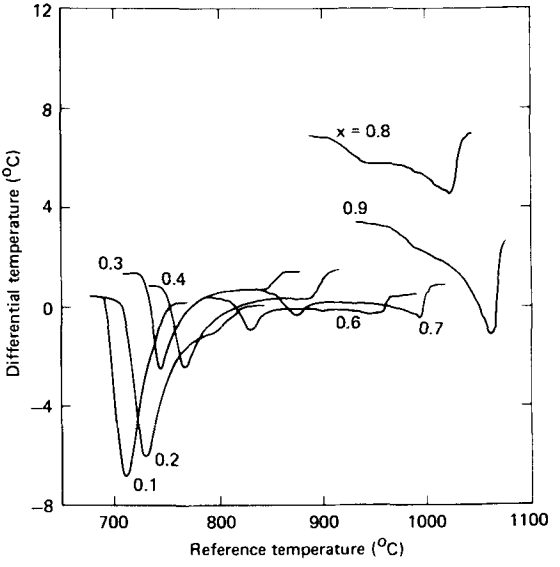

Fig. 7 $Hg_{1-x}Cd_xTe$ melting curves as observed.

A first-order expansion in S/T and P′/T yields

$$T_s \simeq a_1 T + a_2 S - a_3 P', \tag{5}$$

where a_1, a_2, and a_3 are functions of r_q/r_s, ϵ_p/ϵ_s, and ϵ_F/ϵ_s.

For HgTe the empirical correlation between T, S, and T_s is given by

$$T_s = T + 2S - P. \tag{6}$$

For CdTe also, the value of a_2 was found to be 2.

In the case of a nonzero baseline, S_o, T_s is given by

$$T_s = T - S_o + 2S - P. \tag{7}$$

P is primarily the temperature drop across the ampule wall, but this term also includes thermocouple calibration corrections. In the absence of a phase transition, $T_s = T + S_o - P$, that is, the sample temperature is equal to the reference thermocouple temperature plus the differential temperature minus the temperature drop across the ampule wall. For each sample, P was determined by the difference between the observed and actual melting points of the Sb-reference. The values measured for P were 1.3°C to 3.4°C, which agree

reasonably well with those from finite-difference calculations that include both radiation and conduction heat transfer.

The solidus temperatures were determined by replotting the data of Fig. 6 as a function of T_s instead of T, using Eq. (7). The solidus temperatures for $0.1 \leq x \leq 0.7$ were determined by extrapolating the initial, straight-line part of the replotted melting curves to the extended baseline. For $x = 0.8$ and 0.9, the initial departure from the baseline was used because the melting curves had no straight-line sections even when replotted as functions of T_s. The liquidus points, in all cases, were considered to be the temperatures at which the melting curves broke suddenly toward the baseline.

The observed phase equilibrium data are listed in Table II, which includes the observed melting point of CdTe, 1082°C. This value is used for consistency, although previously published values are about 10°C higher.[10]

Each ampule contained a small free-volume. Because the partial vapor pressure of Hg over the alloy melt is much larger than the partial pressures of Cd and Te,[4,5] the preferential evaporation of mercury into the free volume of the ampule alters both the Te/metal and Cd/Hg fractions. An increase in the Te/metal fraction can significantly affect the liquidus temperature as suggested by the decrease of the binary Hg-Te and Cd-Te liquidus temperatures with increasing Te composition immediately above the 50 at.% Te composition.[11-14] The Cd-Te liquidus temperature decreases at $\approx$ 10°C/at.% Te,[12,13] and the Hg-Te liquidus temperature decreases at 1.2°C/at.% Te.[11,14]

The following procedure was used to correct for the small Te-metal excess in the melt resulting from preferential evaporation of Hg into the ampule free-volume. Following alloy casting, the free volume was estimated by measuring the length of the free space in the ampule. The amount of Hg in the gas phase

Table II. Measured phase-equilibrium data for $Hg_{1-x}Cd_xTe$.

Composition (x)	S_o at solidus (°C)	S_o at liquidus (°C)	P (°C)	Observed solidus temperature (°C)	Observed liquidus temperature (°C)
0	0	0	0.6	670	670
0.1	0.5	−1.5	2.9	690	733
0.2	0.4	−1.0	2.9	706	791
0.3	1.4	0.7	2.9	727	841
0.4	0.9	0.3	3.4	748	882
0.6	0.3	−0.3	1.3	810	952
0.7	0.7	−0.4	2.9	850	990
0.8	6.9	4.6	2.9	904	1022
0.9	3.4	−1.0	2.9	952	1051
1.0	−7.9	−7.9	3.7	1082	1082

was determined by using Steininger's[4] empirical relationship for the Hg partial pressure, p, given by

$$p = p_o \exp(21.732 - T_o/T), \tag{8}$$

where p_o = 1 Pa and T_o = 7149 K. The number of moles of Hg, n_{Hg}, remaining in the melt was obtained by subtracting the amount of Hg in the vapor from the amount loaded into the ampule. The actual Te mole fraction in the melt at the observed liquidus temperature is then $n_{Te}/(n_{Hg} + n_{Cd} + n_{Te})$, where n_{Cd} and n_{Te} are the moles of Cd and Te in the melt. The relatively small amounts of Cd and Te_2 in the vapor were neglected, and the values of n_{Cd} and n_{Te} were assumed to be the same as originally placed in the ampule. The observed liquidus temperatures were then corrected by an amount T_c calculated from the expression

$$T_c = \left[\frac{n_{Te}}{n_{Hg} + n_{Cd} + n_{Te}} - 0.5 \right] (1.2 + 8.8x), \tag{9}$$

which is based on a linear interpolation between Hg-Te and Cd-Te of the rate of change of the liquidus temperature with respect to the Te concentration for Te mole fractions slightly above 0.5. The corrections are summarized in Table III.

Table IV lists the liquidus and solidus temperatures determined in this investigation. Table IV also gives the corrected x-values based on $x = n_{Cd}/(n_{Cd} + n_{Hg})$. The composition dependences of the liquidus and solidus temperatures are shown in Fig. 8. The supercooling temperatures in Table IV give the difference in temperature between the liquidus temperatures and the baseline departure of the cooling curves (see Figs. 4 and 5).

Table III. Free-volume correction parameters and corrected liquidus temperatures.

Cd composition (x)	Capsule free volume (cm^3)	Te fraction (%)	Liquidus temperature correction (°C)	Observed liquidus temperature (°C)	Corrected liquidus temperature (°C)
0.1	0.19	50.02	0	733	733
0.2	0.26	50.04	0.1	791	792
0.3	0.69	50.11	0.4	841	841
0.4	0.88	50.21	1.0	882	884
0.6	0.96	50.33	2.1	952	954
0.7	0.74	50.27	2.0	990	992
0.8	1.46	50.31	2.5	1022	1025
0.9	0.87	50.20	1.9	1051	1053

Table IV. Liquidus and solidus temperatures for $Hg_{1-x}Cd_xTe$.

Normal composition (x)	Actual composition at solidus (x)	Solidus temperature (°C)	Actual composition at liquidus (x)	Liquidus temperature (°C)	Supercooling (°C)
0	0	670	0	670	9
0.1	0.100	690	0.100	733	14
0.2	0.200	706	0.200	792	11
0.3	0.301	727	0.302	841	10
0.4	0.402	748	0.404	884	11
0.6	0.604	810	0.607	954	14
0.7	0.704	850	0.707	992	24
0.8	0.806	904	0.810	1025	19
0.9	0.905	952	0.907	1053	30
1	1	1082	1	1082	7

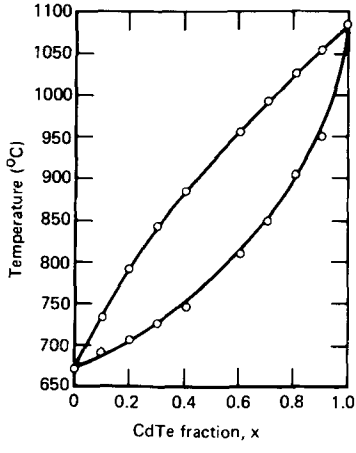

Fig. 8 $Hg_{1-x}Cd_xTe$ phase diagram.

Error Analysis and Comparison with Previous Results

The major recognized sources of error in the phase diagram data are the thermocouple calibrations, the subjectivity in selecting the proper phase-transformation points from the DTA curves, and the uncertainties in the ampule free-volume corrections.

Because the Sb melting point (630.7°C) was used to calibrate the thermocouples during each DTA run, the calibration should be quite accurate near that temperature, although it may be less accurate with increasing temperature.

A type-K thermocouple calibrated at 630.7°C should be accurate to within ±2°C up to 930°C.[8,15] In tests of three different thermocouple combinations used during this investigation, the measured melting temperature of a Ag standard sample differed from the IPTS-68 value of 962°C by not more than ±3°C. Therefore, the expression $3(T - 631°C)/(930 - 631)$ was used as the calibration uncertainty at temperature T, which is equivalent to an uncertainty at the Ag melting point of 3.3°C and is considered adequate to include any graph-paper calibration errors as well as thermocouple calibration errors. For each sample, the calculated uncertainties arising from the temperature measurement uncertainties are listed in Table V.

The second potential source of error is in determination of the critical points of the DTA curves. For the solidus points, the extrapolation of the S vs T_S curve to the baseline for alloys with $0.1 \leq x \leq 0.7$ and the choice of the onset of deviation from the baseline for alloys with $x = 0.8$ or 0.9 are somewhat subjective. Similarly, there were uncertainties in identifying the liquidus points. The latter uncertainties were about 1°C except for the $x = 0.1$ sample, where the liquidus onset occurred in a region of steep slope, and for the $x = 0.8$ and 0.9 samples, for which the liquidus onset was somewhat rounded, as shown in Fig. 6. Estimates of subjectivity in reading the DTA curves are given in Table V under the columns headed "Reading DTA Curve." The uncertainties listed for the free-volume corrections are 25% of the total free-volume corrections.

The total uncertainties listed in Table V are the sums of the individual uncertainties and are believed to represent the maximum possible errors in the reported phase equilibrium temperatures.

The solidus and liquidus temperatures are compared with the results of previous investigations in Fig. 9. The data of Ray and Spencer[1] and Blair and

Table V. Uncertainties of the solidus and liquidus temperatures.

	Solidus temperatures			Liquidus temperatures			
Composition (x)	Temperature calibration (°C)	Reading DTA curve (°C)	Total (°C)	Temperature calibration (°C)	Reading DTA curve (°C)	Free volume effect (°C)	Total (°C)
0.1	0.6	1	1.6	1.0	3	0	4.0
0.2	0.8	1	1.8	1.6	1	0	2.6
0.3	1.0	1	2.0	2.1	1	0.1	3.2
0.4	1.2	1	2.2	2.5	1	0.3	3.8
0.6	1.8	2	3.8	3.2	1	0.5	4.8
0.7	2.2	1	3.2	3.6	1	0.5	5.1
0.8	2.7	3	5.7	3.9	2	0.6	6.6
0.9	3.2	5	8.2	4.2	2	0.5	6.7

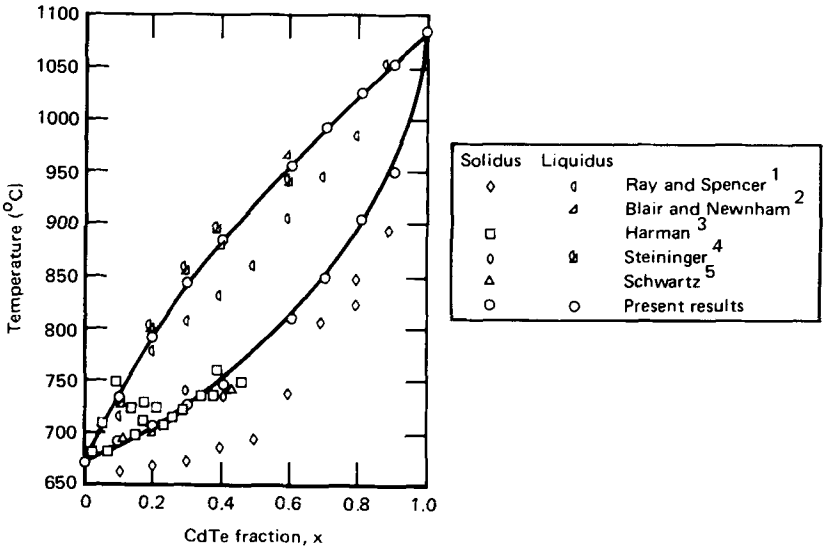

Fig. 9 Comparison of present phase-equilibrium data with previous results.

Newnham[2] were derived from DTA measurements. Harman's[3] data are from chemical analyses of first-to-freeze regions of molten alloy samples. Steininger's[4] data were derived from thermal analyses of samples in a high-pressure apparatus.

A DTA measurement tends to yield a solidus temperature that is too low because of possible inhomogeneities in the sample, whereas the first-to-freeze method tends to yield an x value that is too low for a given temperature. Therefore, on a temperature-composition plot, a solidus curve determined by the first-to-freeze compositions should fall at or above the true curve, and one determined by DTA measurements should fall at or below the true curve. In the present case, the DTA data establish a solidus curve that nearly coincides with the lower limit of Harman's first-to-freeze data, and the two independent sets of data thus are corroborative.

For most compositions, the solidus and liquidus temperatures determined by this investigation are much larger than those reported by Ray and Spencer.[1] A possible explanation for the discrepancies is advanced in Ref. 16.

Liquid-Solid Equilibrium Parameters

The equilibrium temperatures in Table V were used to calculate the temperature and composition dependence of the liquid/solid interface distribution coefficient, $k(T) = x^s(T)/x^l(T)$, where x^s and x^l are the solidus and liquidus compositions. To facilitate the calculations, analytical expressions were developed for $x^s(T)$ and $x^l(T)$. The following functional forms were used:

$$x^s(T) = C_1 \sin\left(\frac{\pi}{2} T^*\right) + C_2 \sin\left(\frac{\pi}{2} T^{*1/2}\right) + C_3 \log_{10}(9T^* + 1) + C_4 T^{*1/2} \qquad (T \geq 690°C) \tag{10a}$$

$$x^s(T) = x^s(690°C)\,(T - 670°C)/20°C \qquad (T < 690°C) \tag{10b}$$

and

$$x^l(T) = D_1 T^* + D_2 T^{*2} + D_3 T^{*3} + D_4 T^{*4}, \tag{11}$$

where $T^* = (T - 670°C)/412°C$ and C_i and D_i are constants. In Figs. 8 and 9, the solid curves are plots of Eqs. (10) and (11) for the values of C_i and D_i given in Table VI. The calculated values of k(T) are shown in Figs. 10 and 11 as functions of temperature and $x^s(T)$, respectively. For small x ($x \leq 0.1$), k is approximately equal to $(dx^s/dT)/(dx^l/dT)$ at $x = 0$. The uncertainties for the low-x phase diagram measurements in Table V imply an uncertainty in k of ± 0.5 at $x = 0$. Within experimental uncertainty, the k values given in Figs. 10 and 11 agree with those which would be obtained from the solid lines in Fig. 15.5 of Ref. 3.

To compare the observed DTA signals with those expected from the alloy properties, the equilibrium liquid fraction, $M_l(T)$, was determined by using the lever rule, $M_l(T) = [x^s(T) - x_o]/[x^s(T) - x^l(T)]$, and the analytical expressions of Eqs. (10) and (11) for x^s and x^l. The temperature derivatives of $M_l(T)$ are shown in Fig. 12 for the indicated compositions.

Figure 13 shows the observed, normalized DTA signals for the various alloy compositions. A comparison with Fig. 12 shows a one-to-one correlation between the magnitudes of the DTA signals and the variation of dM_l/dT with composition. Even the bimodal character of the $x = 0.6$ and 0.7 DTA curves is predicted by the variation of dM_l/dT with temperature. Thus, in principle, if the heat transfer characteristics of the furnace/sample system were known, the compositional and temperature variations of dM_l/dT and thus $M_l(x^s, x^l, x_o)$ could be calculated from the measured thermal-arrest curves and vice versa. However, meaningful deconvolutions of the measured DTA curves

Table VI. Values used for the constants C_i and D_i.

i	C_i	D_i
1	0.502804	0.607640
2	0.165390	0.077209
3	0.746318	0.696167
4	−0.413546	−0.381683

would require a precise thermal model for the sample/furnace system. Approximate heat-transfer calculations were nevertheless performed, and, in general, the calculated and observed DTA curves for the various alloy compositions were comparable. As expected, the detailed features of the calculated curves were sensitive to small variations in the values of the heat-transfer parameters, some of which are not known precisely.

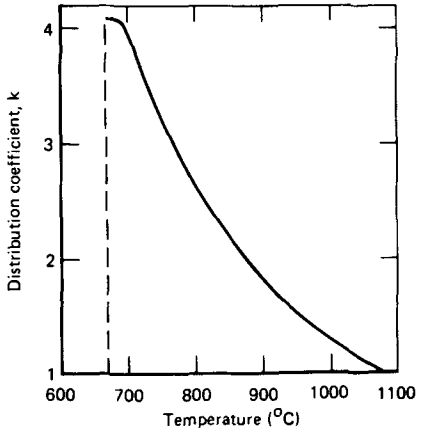

Fig. 10 Temperature dependence of the interface distribution coefficient.

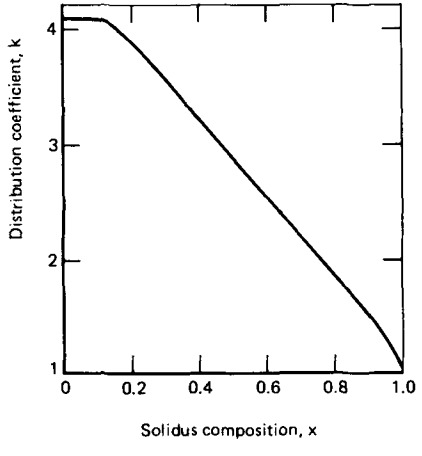

Fig. 11 Composition dependence of the distribution coefficient. At $x = 0$ the uncertainty in k is $\pm$ 0.5.

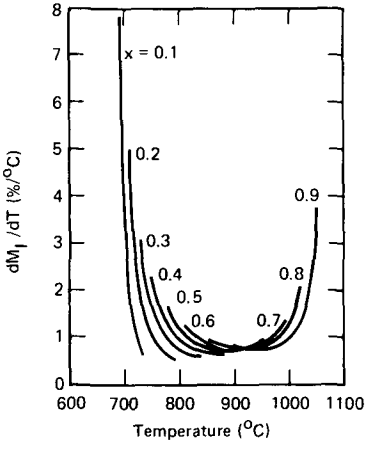

Fig. 12 Temperature dependence of the rate of change with respect to temperature of the alloy liquid fraction for various alloy compositions.

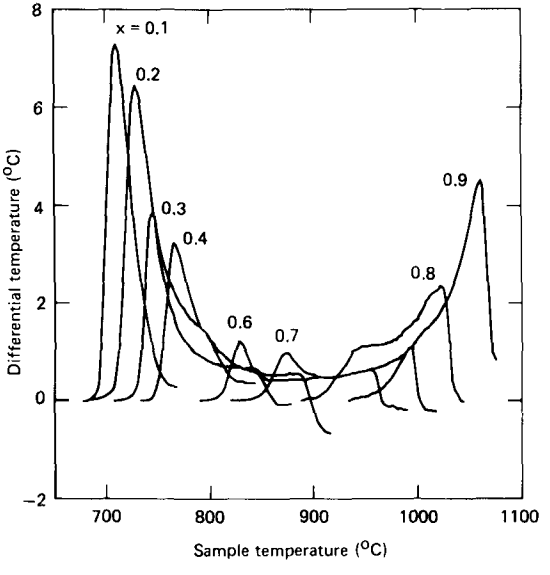

Fig. 13 Compositional variation of the observed DTA signals as functions of sample temperature.

Acknowledgements

The authors are grateful to NASA Marshall Space Flight Center for support of this work. Technical discussions with Drs. M. Davidson, D. Gillies, L. Holland, and C. R. Whitsett were helpful.

References

1. *B. Ray and P. M. Spencer, Phys. Stat. Sol.* **22,** *371 (1967).*
2. *J. Blair and R. Newnham,* ***Metallury of Elemental and Compound Semiconductors,*** *(Interscience Publishers, New York, 1961), Vol. 12, p. 393.*
3. *T. C. Harman, in* ***Physics and Chemistry of II-VI Compounds,*** *M. Aven and J. S. Prener, Eds., (North Holland Publishing Co., Amsterdam, 1967), p. 785.*
4. *J. Steininger, J. Electron. Mater.* **5,** *299 (1976).*
5. *J. P. Schwartz, "A Thermodynamic Investigation of the Ternary Alloy* $(Hg_{1-x}Cd_x)_yTe_{1-y}$ *Using Vapor Phase Spectroscopy," Ph.D. Thesis, Marquette University (1977); available from University Microfilms International, Ann Arbor, MI, UMI-78-10294.*
6. *V. G. Smith, W. A. Tiller, and J. W. Rutter, Can. J. Phys.* **33,** *723 (1953).*
7. *S. L. Lehoczky, F. R. Szofran, and B. G. Martin, "Advanced Methods for Preparation and Characterization of Infrared Detector Materials," McDonnell Douglas Report MDC Q0717, NASA Contract NAS8-33107 (July 1980).*
8. *Methods of Testing Thermocouples and Thermocouple Materials, National Bureau of Standards Circular 590, 1958.*
9. *M. J. Brau, M. J. Williams, J. P. Smith, "Manufacturing Methods for Production of Single-Crystal Mercury Cadmium Telluride," Technical Report AFML-TR-73-88, May 1973.*
10. *D. deNobel, Philips Res. Rep.* **14,** *361 (1959); M. R. Lorenz, J. Phys. Chem. Solids* **23,** *939 (1962); and B. M. Kulwicki, "The Phase Equilibria of some Compound Semiconductors by DTA Calorimetry" Ph.D. Thesis, University of Michigan, School of Engineering (1963).*
11. *A. J. Strauss, M.I.T. Lincoln Lab., private communication.*
12. *M. R. Lorenz, J. Phys. Chem. Solids* **23,** *939 (1962).*
13. *J. Steininger, A. J. Strauss, and R. F. Brebrick, J. Electrochem. Soc.* **117,** *1305 (1970).*
14. *R. F. Brebrick and A. J. Strauss, J. Phys. Chem. Solids* **26,** *989 (1965).*

15. *ASTM Standard E220-72.*

16. *J. L. Schmit and C. J. Speerschneider, Infrared Phys.* **8,** *247 (1968).*